Composites Part B 313 (2026) 113409

Contents lists available at ScienceDirect

Composites Part B

journal homepage: www.elsevier.com/locate/composites

Experimental and numerical investigation of bio-inspired CFRP structures with layer thickness gradients

Marcel Neubacher [a,*], Farida Touni [a], Kohei Yamada [b], Masaaki Nishikawa [c], Bodo Fiedler [a]

[a] Institute of Polymers and Composites, Hamburg University of Technology, Denickestraße 15, 21073 Hamburg, Germany
[b] Industrial Technology Center of Fukui Prefecture, Kawaiwashizuka 61-10, Kawaiwashizuka, 910-0102, Fukui, Japan
[c] Department of Mechanical Engineering and Science, Kyoto University, Kyotodaigaku-katsura C3, Nishikyo-ku, 615-8540, Kyoto, Japan

ARTICLE INFO

Keywords:
CFRP
Finite element analysis
Impact
Out-of-plane
Thin-ply

ABSTRACT

Throughout evolutionary history, mineralised tissues have developed remarkable skeletal microstructures that combine exceptional damage tolerance with adaptation to challenging environmental conditions. These tissues typically feature composite architectures with spatially varying fibre orientations and layer thicknesses.

This study utilises the microstructure of deep-sea sponge spicules and the cuticle of the lobster Homarus americanus as bioinspiration. Sponge spicules, found at depths between 1100 m and 2100 m, consist of radially arranged layers of hydrated silicon dioxide. Their curvature adapts to ocean currents, and analyses reveal graded layer thickness from 0.6 μm to 10 μm. Thinner layers in tensile regions enhance tensile strength due to scaling relationship with layer thickness $h^{-1/2}$, while thicker layers in compressive zones improve stability and reduce buckling. Unlike this microstructure, the cuticle of Homarus americanus comprises epicuticle, exocuticle, and endocuticle, with the latter two forming helicoidal fibre architecture. In the claws, exocuticular layers are thinner, facilitating energy absorption under impact, whereas thicker endocuticular layers provide structural stabilisation through increased stiffness.

Inspired by these biological systems, thin-ply carbon fibre reinforced polymer laminates were designed for out-of-plane loading conditions. A quasi-isotropic layup $[45°, 90°, -45°, 0°]$ was chosen to reflect amorphous nature of hydrated silica. To mimic natural gradients, layers of varying thin-ply thickness were employed within thermally balanced laminate sequence. Layer configurations were initially optimised using finite element three-point bending simulations and subsequently validated experimentally.

The graded design approach resulted in improved flexural performance and reduced damage propagation under impact loading, demonstrating potential of bio-inspired layer thickness gradation for development of advanced composite structures.

1. Introduction

During the course of mineralised tissue evolution, nature has created remarkable skeletal microstructures that demonstrate excellent resistance to damage and are ideally adapted to a wide range of challenging environmental conditions. These mineralised tissues are characterised by a composite structure with varying angles and different layer thicknesses [1–6]. Such composite structures can be observed in fish, crustaceans, and sponges. Inspired by these biological structures, the present work investigates a graduated design approach for carbon fibre reinforced polymers (CFRPs) that adapts these natural concepts to technical laminates.

Translating these bio-inspired, layered architectures into technical applications requires a high degree of design flexibility, especially with respect to the arrangement and thickness of individual layers. This design freedom is enabled through the use of thin-layer carbon fibre reinforced polymers (CFRPs), so-called thin-plies, which are manufactured using spread-tow processes among other methods and represent a high-performance alternative to conventional prepregs. Prepregs with a thickness of 100 μm or less are called thin-ply and can be made as thin as 20 μm using current manufacturing methods [7–9].

In addition to offering greater design freedom by allowing a greater number of thinner layers to be stacked and precisely orientated, thin-ply laminates also exhibit increased in-situ strength, since damaging mechanisms such as transverse microcracking or delamination at free edges are suppressed [7]. As a result, there is a transition in failure

* Corresponding author.
E-mail address: marcel.neubacher@tuhh.de (M. Neubacher).

https://doi.org/10.1016/j.compositesb.2026.113409
Received 20 November 2025; Received in revised form 19 December 2025; Accepted 11 January 2026
Available online 12 January 2026

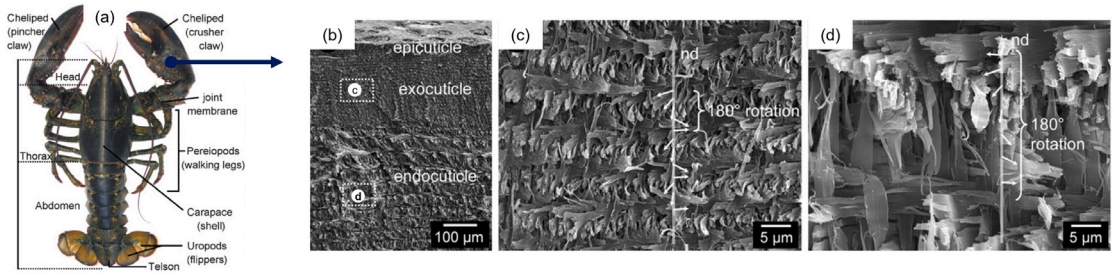

Fig. 1. (a) Lobster homarus americanus; (b) SEM image depicting a cross-sectional view of the microstructure of the lobster cuticle; (c) SEM magnification of the exocuticle; (d) SEM magnification of the endocuticle [4].

behaviour from delamination-dominated failure modes in thick layers to more brittle, fibre-based failure types in thin layers. This leads to increased tensile and compressive strength in quasi-isotropic and unidirectional laminates [9–12].

In [13], the compressive behaviour of QI laminates with varying fibre areal weights was investigated. The measured compressive strengths were 565.63 MPa for thick layers (240 g/m^2), 610.39 MPa for medium layers (120 g/m^2) and 690.73 MPa for very thin layers (30 g/m^2). Thus, the compressive strength of QI laminates continuously increases as the thickness of the layer decreases. The authors attribute this to increased bending stiffness of the laminate, as more fibres with a 0° orientation are arranged further away from the centre of the middle layer. The increased bending stiffness thus improves both the global and local stability of the laminate. This effect counteracts bending deformation and reduces uneven loads, thus reducing the risk of premature failure.

Under tensile load, the fibre areal weights have a clear influence. For quasi-isotropic laminates, the tensile strengths of 847 MPa at 30 g/m^2, 832 MPa at 100 g/m^2 and only 595 MPa at 300 g/m^2 were determined [12]. The authors attribute these results to the increased homogeneity of the microstructure and the reduced incidence of interfacial effects in thinner layers. Arteiro et al. [9] also report improved manufacturing quality in the production of thin-ply laminates. This is particularly evident in lower pore content, optimised fibre orientation, and a reduction in resin-rich zones.

Due to the different damage behaviour of thin and thick-layers, the combination of different layer thicknesses in symmetrical laminate structures has already been the focus of previous research work [14–20].

The publications [18] and [19] deal with the combination of different layer thicknesses and investigate their influence on behaviour under impact and CAI loads. In [18], it was shown that the CAI strength can be increased by 31 % through a symmetrical arrangement of thin and thick layers. A very similar effect was also observed in [19]. In the case of symmetrical laminate structures with varying layer thicknesses, an improvement of up to 40 % was achieved compared to the reference material [19].

The studies by [16] and [17] investigated thick-thin-thick-ply laminates with quasi-isotropic layup configurations and conducted both compression after impact (CAI) and short beam shear (SBS) tests. Li et al. [17] demonstrated that laminate structures with symmetrical graduated ply thicknesses resulted in a 29 % increase in dissipated energy compared to reference laminates composed of uniform 120 µm ply thickness. Furthermore, the symmetrically graduated layup led to a 52.9 % reduction in damage area. Concurrently, the residual compressive strength was enhanced by 18.5 % compared to reference laminates 120 µm and by 14.4 % compared to laminates with 30 µm ply thickness. The authors observed that the graded layup exhibited a delamination behaviour similar to that of fully thin-ply laminates, while simultaneously improving the CAI strength. Additionally, [16] reported that a symmetric thick-thin-thick ply design incorporating ultra-thin plies in the mid-plane effectively suppressed delamination and consequently achieved the highest shear strengths.

Sasikumar et al. [21–23] analysed a graduated asymmetric layer structure in which layers of different thicknesses were combined throughout the laminate thickness. However, these investigations were limited to structures with relatively small thickness differences (i.e. double-ply thickness) and did not present an universally applicable design approach. The structures were subjected to an impact test, after which their residual compressive strength was determined. The laminate with a graduated design, in which the thin layers are arranged on the impact side and the thicker layers are arranged away from the impact side, shows a significantly reduced extent of fibre damage. In addition, the damaged area is reduced by approximately 50 % compared to the thin-ply structure. Due to its improved impact behaviour, the asymmetric graduated laminate achieves an increase in CAI strength of approximately 30 % compared to the thin-layer reference laminate [21].

Although these technical studies demonstrate the potential benefits of combining thin- and thick-layers, as well as graduated layer thicknesses in composites, they often rely on empirical approaches or limited variations in thickness gradients. In contrast, mineralised materials have evolved highly optimised structures in which variations in layer thickness and fibre orientation are perfectly adapted to environmental challenges.

In crustaceans, the exoskeleton comprises the endocuticle on the inside, the exocuticle in the middle, and the epicuticle on the outside, as shown in Fig. 1(a)–(b). The epicuticle serves mainly to protect against external influences. The endocuticle and exocuticle, on the other hand, are primarily responsible for absorbing mechanical loads. Within the endocuticle and exocuticle, crustaceans have a fibre-reinforced composite structure in which chitin fibres are embedded in a protein-containing matrix. These layers are arranged in a helical pattern, also known as a Bouligand structure. Such structures are found, among other places, in the claws of lobsters [4,6], in the shells of beetles [5] and in the dactyl club of mantis shrimp [1]. The helical arrangement leads to damage-tolerant properties and prevents delamination and has been studied extensively in numerous articles [24–30]. In addition to the helical fibre arrangement, crustaceans exhibit variations in the thickness of individual Bouligand units and individual layers. For example, in lobster claws, the fibre layers are thinner in the exocuticle and thicker in the endocuticle [4,6], as illustrated in Fig. 1(c)–(d). In this study, the distinctive thickness variations of the Bouligand units are examined using a commonly used laminate structure.

Zhang et al. [30] proposed a promising approach to replicate the exoskeleton structure of the lobster Homarus americanus by investigating asymmetric hybrid helical structures with varying ply thicknesses and pitch angles, inspired by the exocuticle and endocuticle architecture. Their results show that combining a large pitch angle with thin plies on the upper side and a small pitch angle with thick plies on the lower side significantly enhances damage resistance and protective performance. Thin plies and large pitch angles contribute to higher knee load capacity, while thick plies and small pitch angles improve energy absorption.

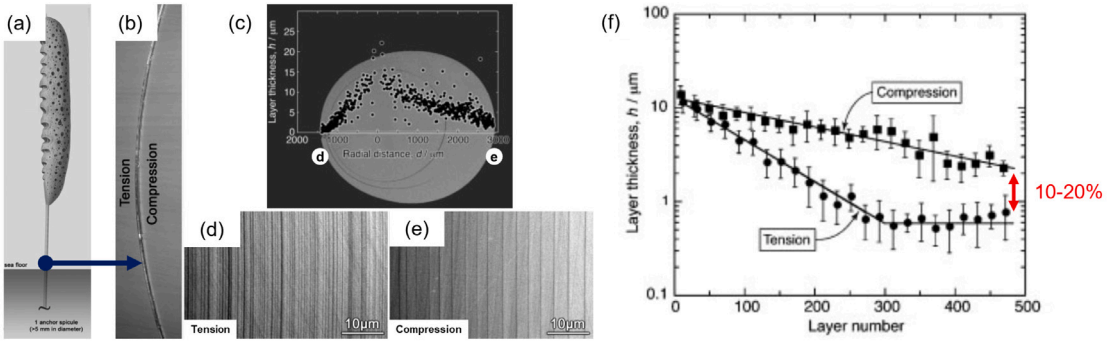

Fig. 2. (a) Monorhaphis Chuni belongs to the genus of sponge spicules; (b) Anchor spicule of monorhaphis chuni; (c) Graph showing silica layer thickness as a function of distance from the spicule centre along the bending axis (d) Magnified view of the tensile region of the thin layer in the anchor spicule (e) Magnified view of the compression region of the thick layer in the anchor spicule; (f) Thickness of the silica layers changes with the layer number, counted from the spicule's centre [2].

This hybrid design, which follows the biological design concept of the lobster Homarus americanus, outperforms uniform helical structures by simultaneously increasing strength and energy dissipation. The study highlights ply hybridisation and pitch angle variation as a promising strategy to improve the damage tolerance of thin-ply composites under out-of-plane loading.

The sponge spicules represent another mineralised structure characterised by varying layer thicknesses. An example of Monorhaphis Chuni, the sponge spicule species studied in this work, is shown in Fig. 2(a). These marine sponge species are anchored to the sea floor at a depth of 1100 m and 2100 m by a round or oval anchor spicule with a diameter greater than 5 mm. The anchor spicule has a multilayered structure of hydrated silicon dioxide, which is isotropic in structure. Between the individual layers is a protein-like material that acts as a crack stopper. This structural and functional principle was studied in detail by [2]. It was found that the layer structure has different thicknesses (0.6 µm to 10 µm). The alignment of the needle system along the ocean current ensures that the thinner layers are predominantly located in the tension zone, while the thicker layers are mainly positioned in the compression zone. This is illustrated in Fig. 2(b)–(f). The thickness of the thin layers is approximately 10 % to 20 % of that of the thicker layers, as shown in Fig. 1(f). The distribution of layer thickness across the cross-section in the tensile and compressive zones, measured from the centre of the anchor spicule, is illustrated in Fig. 2(c)–(f). This ratio can be explained by two key mechanical effects. Firstly, a reduction in layer thickness leads to an increase in tensile stress, which increases according to a scaling factor of $h^{1/2}$, where h represents the layer thickness. Second, thicker layers prevent buckling in the compression zone, improving overall structural stability [2,3].

Greenfeld et al. [31] analysed crack propagation in the cuticle of scorpions, as well as in the sponge's spicule. It was demonstrated that these mineralised structures are characterised by a stepwise crack propagation that results in a layer-wise crack growth that transitions to delamination at the layer interfaces and subsequently leads to crack initiation in the adjacent layer.

The microstructures shown in Figs. 1 and 2 provided the inspiration for this study. Taking into account the amorphous nature of sponge spicules made of hydrated silicon dioxide together with the Bouligand structure of the lobster Homarus americanus which displays almost isotropic behaviour in the plane at small pitch angles, a quasi-isotropic laminate orientation with angles 0°, −45°, 90° and 45° was chosen [2,3]. This quasi-isotropic fibre arrangement is one of the most commonly used configurations in industrial applications.

Both biological animals, exemplified by lobsters and sponge spicules, show differences in thickness within their layer structures, but these differences are opposite in nature. Although the thinner layers of sponge spicules are predominantly located in the tensile zone, the layers of lobster in the endocuticle, which are subjected to tensile stress when loads are applied out of plane, tend to be thicker [2,4,6]. Based on the thickness ratios of sponge spicules, where thin layers reach approximately 10 % to 20 % [2] of the thickness of thicker layers, thin layers with a base weight of 30 g/m^2 and thick layers with 300 g/m^2 were defined in this work. Both phenomena involving thin layers in the tensile zones and thick layers in the tensile zones were taken into account in the structural design. Graded structures typically exhibit asymmetry with respect to the classical laminate theory, which motivated the development of a generalised design approach specifically for graded asymmetric structures.

To investigate the properties of these graded designs structures, three-point bending tests were established as the primary loading mode, reflecting the dominant type of load experienced by sponge spicules. Based on this, finite element simulations of three-point bending were conducted to evaluate the advantages of graded structures. The simulation results were then experimentally validated and complemented by additional loading scenarios commonly found in nature, such as impact and shear stresses. Consequently, the out-of-plane properties were characterised through interlaminar shear stress and compression after impact testing (CAI).

2. Materials and methods

2.1. Materials and specimen preparation

The test samples were prepared using unidirectional prepreg materials supplied by North Thin Ply Technology (NTPT), consisting of Toray T700SC-12K-60E carbon fibres embedded in NTPT ThinPreg 402 epoxy resin. Two types of fibre areal weights 30 g/m^2 and 120 g/m^2 were utilised. The fibre volume fractions for these prepreg and fibre areal weights, reported in a previous publication [13], were determined as 57.80 ± 0.51 % for 30 g/m^2 and 56.07 ± 0.57 % for 120 g/m^2. Given the small difference between these values, the material properties were assumed to be identical for both the analytical design approach and the simulation in the present study. All other intermediate areal weights, as specified in Tables 1, 3 and illustrated in Fig. 3, were obtained using a block-scaling approach, meaning that several layers of the base prepregs were stacked to achieve the desired layer areal weight. For example, a 60 g/m^2 configuration was obtained by stacking two 30 g/m^2 layers, while a 180 g/m^2 configuration was produced by combining one 120 g/m^2 layer with two 30 g/m^2 layers. The laminate architectures detailed in Table 1 were manually stacked using a hand lay-up technique, followed by consolidation in an autoclave under process parameters recommended by the manufacturer.

After curing, all laminate panels were subjected to ultrasonic C-scan inspection by using USPC 3040 ultrasonic testing system (Ingenieurbüro Dr. Hillger) to identify potential manufacturing defects prior to

Table 1
Overview of the investigated configurations, including layup details, layer areal weight and nominal specimen thicknesses h.

Configuration	Layup	Layer areal weights	h in mm
30 g/m^2	$[0,-45,90,45]_{17s}$	30 g/m^2	4.08
30–300 g/m^2	$[0,-45,90,45]_1$	30 g/m^2	4.08
	$[0,-45,90,45]_1$	60 g/m^2	
	$[0,-45,90,45]_2$	90 g/m^2	
	$[0,-45,90,45]_1$	120 g/m^2	
	$[0,-45,90,45]_1$	150 g/m^2	
	$[0,-45,90,45]_1$	180 g/m^2	
	$[45,90,-45,0]_1$	300 g/m^2	
300–30 g/m^2	$[0,-45,90,45]_1$	300 g/m^2	4.08
	$[45,90,-45,0]_1$	180 g/m^2	
	$[45,90,-45,0]_1$	150 g/m^2	
	$[45,90,-45,0]_1$	120 g/m^2	
	$[45,90,-45,0]_2$	90 g/m^2	
	$[45,90,-45,0]_1$	60 g/m^2	
	$[45,90,-45,0]_1$	30 g/m^2	
300 g/m^2	$[0,-45,90,45]_{2s}$	300 g/m^2	4.80

testing. No manufacturing-related defects were detected in the panels. The laminates were sectioned into test coupons using a Brillant 265 precision circular saw (ATM Qness GmbH), equipped with a diamond blade and operated with a constant feed rate of 1.0 mm s^{-1} under water cooling to minimise thermal effects. All specimen edges were subsequently polished using abrasive paper with a grit size of P1000 to achieve clean and reproducible surfaces. Before mechanical characterisation, all samples underwent a conditioning process in a vacuum oven at 40 °C for 48 h, ensuring comparable material behaviour. Mechanical testing was conducted under controlled laboratory conditions (20 °C, 50 % relative humidity).

To analyse the failure mechanisms and internal structure of the laminates, the selected fracture surfaces were examined using the VHX-6000 digital microscope (Keyence Deutschland GmbH). For this purpose, samples were embedded in KEM15 Plus resin (ATM Qness GmbH), then ground and polished in a multi-stage process on an automated Saphir 550 machine of the same manufacturer. The procedure included sequential grinding starting at 320-grit, finishing with a final polishing step using a 1.0 µm diamond suspension.

2.2. Laminate design

The realisation of asymmetric laminate structures with arbitrary layer-thickness variations required the development of a novel graded design approach. The first steps towards this were already explored by [21–23], who combined layers of varying thickness through the thickness of the laminate. However, these investigations were limited to structures with relatively small thickness differences (0.134 g/m^2 to 0.067 g/m^2) and did not present a universally applicable design approach. In contrast, the present study investigated significantly larger variations in layer thicknesses, necessitating the formulation of a generalised design approach to combine layers of variable thickness within a graded structure.

In the design of fibre-reinforced polymer laminates, it is generally required that the coupling matrix (B-matrix) of the ABD-matrix in classical laminate theory, which describes coupling effects between extension and bending, should ideally be zero. Although this condition was inherently satisfied by classical symmetric laminates, it was typically not satisfied for graded asymmetric laminates. This observation formed the basis for developing a general design methodology aimed at deliberately realising asymmetric, graded laminate structures that nonetheless preserved symmetry concerning the B-matrix.

The theoretical concept was based on an arbitrary laminate structure with two angle-ply combinations X and Y, combined with differing ply thicknesses t_{k1} and t_{k2}, and repetition factors m and n:

$$[X,Y]_{m-t_{k1}}\,[Y,X]_{n-t_{k2}} \tag{1}$$

Table 2
Ratio of repetition factors as a function of combined ply thickness variations.

n/m	t_{k1}			
t_{k2}	0.03	0.06	0.09	0.12
0.03	1	4	9	16
0.06	$\frac{1}{4}$	1	$\frac{9}{4}$	4
0.09	$\frac{1}{9}$	$\frac{4}{9}$	1	$\frac{16}{9}$
0.12	$\frac{1}{16}$	$\frac{1}{4}$	$\frac{9}{16}$	1

The total thickness of the laminate h can be determined by relating it to the arbitrary laminate structure defined in Eq. (1). Specifically, considering the repetition factors m and n for the angle-ply combinations with respective ply thicknesses t_{k1} and t_{k2}, the total laminate thickness is calculated as shown in Eq. (2):

$$h = 2\cdot\left(m\cdot t_{k1} + n\cdot t_{k2}\right) \tag{2}$$

To avoid coupling between stresses and moments, all entries in the B-matrix had to vanish according to Eq. (3):

$$\mathbf{B} = \frac{1}{2}\sum_{k=1}^{n}\bar{\mathbf{Q}}_k\cdot\left(z_k^2 - z_{k-1}^2\right) = \sum_{k=1}^{n}\bar{\mathbf{Q}}_k\cdot t_k\left(z_k - \frac{t_k}{2}\right) = 0 \tag{3}$$

Assuming that the layer thickness does not affect the $\bar{\mathbf{Q}}_k$ matrices at a constant angle, the following relationship can be derived from Eq. (3):

$$\mathbf{B} = \bar{\mathbf{Q}}_X\cdot S_X + \bar{\mathbf{Q}}_Y\cdot S_X\ : \tag{4}$$

where S_X and S_Y represent the sums of all terms $t_k\left(z_k - \frac{t_k}{2}\right)$ corresponding to the respective angles. From this, the following expressions for S_X (Eq. (5)) and S_Y (Eq. (6)) are obtained:

$$S_X = t_{k2}\cdot\sum_{i=1}^{n}-\frac{h}{2} + (2\cdot i - 1.5)\cdot t_{k2} + t_{k1}\cdot\sum_{i=1}^{m}\frac{h}{2} - (2\cdot i - 1.5)\cdot t_{k1} \tag{5}$$

$$S_Y = t_{k2}\cdot\sum_{i=1}^{n}-\frac{h}{2} + (2\cdot i - 0.5)\cdot t_{k2} + t_{k1}\cdot\sum_{i=1}^{m}\frac{h}{2} - (2\cdot i - 0.5)\cdot t_{k1} \tag{6}$$

By substituting the overall thickness h from Eq. (2) and employing arithmetic sequences, the following reduced forms are derived:

$$S_X = -0.5\cdot n\cdot t_{k2}^2 + 0.5\cdot m\cdot t_{k1}^2 \tag{7}$$

$$S_Y = +0.5\cdot n\cdot t_{k2}^2 - 0.5\cdot m\cdot t_{k1}^2 \tag{8}$$

Based on Eq. (4) and incorporating the insights of Eqs. (7) and (8), the relationship expressed in Eq. (9) was derived. This relationship, which links layer thicknesses with repetition factors, demonstrates that the selected laminate configuration, characterised by varying thicknesses but consistent angle-ply sequences [X,Y], preserves the symmetry of the B-matrix.

$$\left(\frac{t_{k1}}{t_{k2}}\right)^2 = \frac{n}{m} \tag{9}$$

A generalised approach was formulated for the construction of graded asymmetric laminates, ensuring symmetry with respect to the B-matrix despite variations in layer thickness. Exemplary combination factors for these constructions are presented in Table 2.

Based on this developed design methodology and inspired by biological models, laminate structures with significantly larger differences in layer thickness were realised. The primary inspiration came from a study that analysed the laminate structure of the sponge spicules, which indicated that the thinnest layers were approximately 10 times thinner than the thickest layers [2]. Consequently, for the present study, areal weights of 30 g/m^2 for the thinnest and 300 g/m^2 for the thickest layers

Table 3
Summary of calculations for graded structures with variable ply thicknesses.

Index variable	Layup	Layer areal weights	$n_{i-actual}$	$\left(\frac{t_{ki}}{t_{ki}}\right)^2 = \frac{n_i}{m}$	R	$\left(\frac{n_i}{m}\right)_{corrected}$
i = 1	[0, −45, 90, 45]	300 g/m^2	1	–	–	–
i = 2	[45, 90, −45, 0]	180 g/m^2	1	2.78	0.64	–
i = 3	[45, 90, −45, 0]	150 g/m^2	1	4.00	0.61	2.56
i = 4	[45, 90, −45, 0]	120 g/m^2	1	6.25	0.59	2.44
i = 5	[45, 90, −45, 0]	90 g/m^2	2	11.11	0.22	2.56
i = 6	[45, 90, −45, 0]	60 g/m^2	1	25.00	0.20	1.25
i = 7	[45, 90, −45, 0]	30 g/m^2	1	100.00	–	1.00

were defined. To accommodate such a substantial difference in thickness (factor of 10), which according to Eq. (9) corresponds to a ratio of repetition factors of 100 and thus would result in considerable total laminate thicknesses, intermediate layer thicknesses were integrated into the structure. This facilitated a continuous, gradual transition between thin, intermediate, and thick layers.

To integrate intermediate layer thicknesses, $\frac{n_i}{m}$ must be adapted in dependence on the previous stacked layer thicknesses. For this purpose, a factor R is used, which describes the ratio between the value calculated according to Eq. (9) and the actual number $n_{i-actual}$ of stacked angle-ply combinations [X,Y] (see Eq. (10)).

$$R_i = \begin{cases} 1 - n_{i,\text{actual}} \cdot \frac{n_i}{m}, & \text{for } i = 2 \\ 1 - n_{i,\text{actual}} \cdot \left(\frac{n_i}{m}\right)_{\text{corrected}}, & \text{for } i > 2 \end{cases} \tag{10}$$

The corrected factor $\left(\frac{n_i}{m}\right)_{corrected}$ for the thickness of the subsequent layer can be determined using the factor R calculated in Eq. (10), applying Eq. (11).

$$\left(\frac{n_i}{m}\right)_{corrected} = \frac{n_i}{m} \cdot \sum_{k=3}^{i} R_{k-1} \tag{11}$$

Taking into account the amorphous nature of sponge spicules composed of hydrated silicon dioxide, a quasi-isotropic laminate orientation of $[45°, 90°, -45°, 0°]$ was selected [2,3]. In addition, a reference thickness of 4.08 mm was specified. The laminate configurations investigated in this study are summarised in Table 1. In Table 3, the corresponding input values, as well as the resulting outputs of Eqs. (10) and (11) are shown exemplary for the 300–30 g/m^2 graded configuration from Table 1.

The designations 30–300 g/m^2 and 300–30 g/m^2 indicate graded laminate structures, each representing a mirrored orientation of the other. For out-of-plane tests, the notation implies that the first listed areal weight value is orientated towards the direction of the applied force. In the case of 30–300 g/m^2, the 30 g/m^2 layer is facing the out-of-plane load, while the 300 g/m^2 layer corresponds to the opposite side.

The laminate structures were fabricated using plies with areal weights of 30 g/m^2 and 120 g/m^2, as well as combinations thereof, as explained in Section 2.1. These graded laminate structures are compared to quasi-isotropic (QI) reference laminates constructed entirely from 30 g/m^2 and 300 g/m^2 layers.

The images (a) to (c) in Fig. 3 show micrographs of the laminate configurations listed in Table 1. The respective QI stack structures are highlighted in red. Each QI stack consists of four layers $[45°, 90°, -45°, 0°]$, and the corresponding areal weight per layer is indicated in dark blue below each QI stack. Based on this representation and the fact that no thermal deformations or warping occurred in the plates after autoclave curing, it can be confirmed that the stacking sequences were designed such that the coupling B-terms are effectively zero. This ensures that the laminates remained flat without any curvature or distortion, thus validating the generalised approach formulated in Eq. (9). The position of the neutral axis where both stress and strain are zero was calculated and found to remain at the mid-plane of the laminate since the B-matrix is zero.

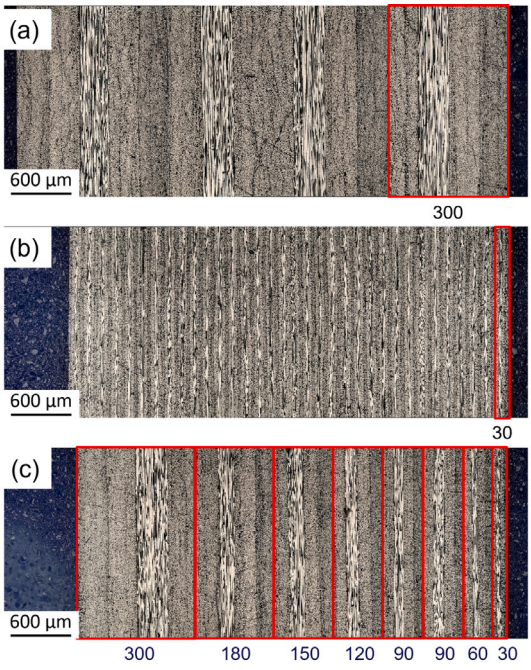

Fig. 3. Micrographs of the laminate configurations listed in Table 1. QI stacks highlighted in red, each composed of four layers with areal weight per layer in g/m^2 shown below; (a) 300 g/m^2; (b) 30 g/m^2; (c) 30–300 g/m^2 & 300–30 g/m^2. (For interpretation of the references to colour in this figure legend, the reader is referred to the web version of this article.)

2.3. Finite element model

The finite element model (FEM) was created using Dassault Systèmes Abaqus/CAE 2023 software. The structure is based on the DIN EN ISO 14125 standard [41] and is shown schematically in Fig. 4. To model the laminate structure, each fibre orientation was defined as a separate layer. The layers were connected to each other using COH3D8 cohesive elements with zero thickness using a traction–separation law to model interlaminar delamination. The mesh used is a structured rectangular mesh without explicit consideration of the fibre angle orientation. The actual sample structure was modelled using C3D8R elements. The pressure and support surfaces (fins) were represented as rigid surfaces by R3D4 elements. The load was applied by a translational movement of the pressure fin in the z-direction, while the two supports were fixed. The load was applied via a velocity profile in the form of a cosine function. A maximum velocity of $v_{\max} = 1 \times 10^{-2}$ mm s^{-1} was selected. The velocity over time t is calculated using the following equation:

$$v(t) = v_{\max} \cdot \left(1 - \cos\left(\frac{\pi \cdot t}{T}\right)\right) \tag{12}$$

Here, T denotes the total duration of the load, which was selected depending on the desired strain and the resulting displacement in the z-direction. The target time increment was set to 10^{-3}. In this

Table 4
Material parameters utilised in the finite element analysis.

Elastic properties					
E_1 (MPa)	E_2 (MPa)	E_3 (MPa)	G_{12} (MPa)	G_{13} (MPa)	G_{23} (MPa)
117 000	8350	8350	3960	3960	2879
[32]	[32]	[32]	[32]	[32]	[32]
ν_{12} (–)	ν_{13} (–)	ν_{23} (–)			
0.38	0.38	0.45			
[32]	[32]	[32]			
Strength and failure parameters					
X_T (MPa)	X_C (MPa)	Y_T (MPa)	Y_C (MPa)	S_L (MPa)	α_0 (Rad)
2333.00	985.00	190.86	163.00	175.99	0.925
[32]	[32]	[33]	[32]	[33]	[34,35]
Plasticity parameters					
f_{XT} (–)	G_{XT} (MPa)	f_{GXT} (–)	f_{XC} (–)	G_{XC} (MPa)	f_{GXC} (–)
0.20	133.30	0.50	0.20	47.50	0.50
[35,36]	[36]	[35,36]	[35]	[37]	[35]
Cohesive properties					
$Y_{T,init}$ (MPa)	$S_{L,init}$ (MPa)	$G_{IC,init}$ (N mm^{-1})	$G_{IIC,init}$ (N mm^{-1})	$\eta_{BK,init}$ (–)	
60.00	80.00	0.25	2.20	1.50	
[38]	[38]	[39]	[39]	[40]	

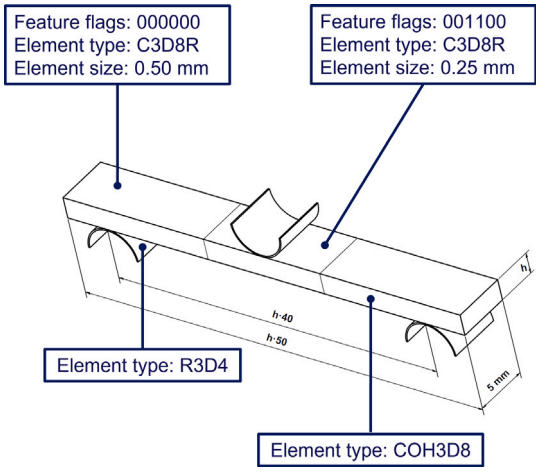

Fig. 4. Schematic structure of the FE model for three-point bending.

work, the CompDam deformation gradient decomposition (DGD) model was implemented as a vector-based user material (VUMAT) [36]. This material model is based on the LaRC04 failure criterion developed by NASA Langley Research Centre [42]. LaRC04 is a three-dimensional failure model for fibre-reinforced composites and is characterised by its ability to realistically represent various damage-relevant mechanisms. These include matrix failure, shear non-linearities, and fibre breakage under tensile and compressive loads, taking fibre buckling into account. In addition, friction effects can be considered. To reduce the calculation time, a damage-tolerant CompDam material model was used in the outer area of the test specimen, in which no damage was taken into account. This was achieved by turning off all the damage variables. In this area, the mesh size was 0.50 mm. However, in the inner area below the pressure fin (see Fig. 4), damage modelling was allowed in tension and compression of the fibre direction. In order to enable a more accurate representation of failure behaviour, the mesh size was reduced to 0.25 mm here. A constant mesh size of 30 µm was used in the thickness direction for all configurations. The initiation and progression of the damage were tracked using internal state variables supplied by the VUMAT, allowing for the detection of the onset of fibre and delamination damage.

In Table 4 all relevant material parameters that were used in the simulation are shown.

2.4. Three-point bending

The flexural properties of the different laminate structures were evaluated in accordance with DIN EN ISO 14125 [41], applying the standard's procedures to both experimental measurements and numerical calculations. Method A of the standard was applied, which corresponds to a three-point bending setup. All tests were performed using a 10 kN universal testing machine (ZwickRoell GmbH & Co. KG) at a constant crosshead displacement rate of 1 % min^{-1}. The material was classified as class IV. To comply with the standard and account for the nominal thickness of the laminate, both the specimen dimensions and the support span were adjusted accordingly. The flexural stress was calculated according to Eq. (13):

$$\sigma_f = \frac{3 \cdot F \cdot L}{2 \cdot b \cdot h^2} \tag{13}$$

where σ_f is the flexural stress, F is the applied force, L is the support span, b is the width of the sample and h is the thickness of the sample. For the calculation of the strain, the crosshead displacement s was used to determine the estimated flexural strain ϵ according to Eq. (14):

$$\epsilon = \frac{6 \cdot s \cdot h}{L^2} \tag{14}$$

2.5. Interlaminar shear strength

The interlaminar shear properties of the laminates were determined according to DIN EN ISO 14130 [43]. All tests were conducted using a 10 kN universal testing machine (ZwickRoell GmbH & Co. KG) at a constant crosshead displacement rate of 1 mm min^{-1}. To ensure compliance with the standard and to account for the nominal laminate thickness, the specimen dimensions and support span were adjusted accordingly, as the manufactured panels exceeded the desired thickness of the standard test geometry.

The apparent interlaminar shear strength τ was determined from the recorded force–displacement data using Eq. (15):

$$\tau = \frac{3}{4} \cdot \frac{F}{b \cdot h} \tag{15}$$

where F is the applied force, b is the width of the specimen, and h is the thickness of the specimen.

2.6. Compression after impact

Compression after impact (CAI) tests were conducted in accordance with ASTM D7136-05 to evaluate the residual compressive strength of the impacted specimens [44]. First, low-velocity impact events were

introduced using an Instron 9450 drop tower equipped with a semi-spherical impactor of 20 mm diameter. The impactor mass was 4.535 kg. The impact energy per unit thickness was controlled and set to approximately 3.3 J mm^{-1}, based on the actual measured thickness of each specimen. For each laminate configuration, two specimens were subjected to impact loading.

After impact, all samples were examined for internal damage by ultrasonic inspection in a water bath to assess the extent of delamination and other defects. The inspections were performed with the USPC 3040 ultrasonic testing system (Ingenieurbüro Dr. Hillger) and software developed by the Institute of Polymers and Composites was used to evaluate the data.

Subsequently, the residual compressive strength was determined using a ZwickRoell Z400 testing machine (maximum load capacity: 400 kN) according to the procedure specified in ASTM D7137-05 [45]. The residual compressive strength after impact was determined in accordance with the standard using the following equation:

$$\sigma_c = \frac{|P_{max}|}{b \cdot h} \tag{16}$$

where $|P_{max}|$ denotes the absolute value of the maximum compressive load, b is the width of the sample and h is the thickness of the sample.

3. Results and discussion

3.1. Three-point bending tests

All of the determined material property data related to the flexural tests, including mean values and standard deviations, are summarised in Table A.7. In the following Fig. 5(a) the results of the numerical three-point bending tests are shown in a stress–strain diagram. This shows that the reference material 30 g/m^2 and the bio-inspired laminate 30–300 g/m^2 show similar behaviour and the highest flexural strength, whereby the bio-inspired configuration only have 32 layer compared to 136 layer of the 30 g/m^2. The configurations 300 g/m^2 and 300–30 g/m^2 exhibited the lowest strength values in numerical analyses. The numerical simulations illustrate the potential of graded structures and provides valuable information on their mechanical behaviour. Based on these results, supplementary experimental investigations were carried out to validate the numerical predictions and analyse the behaviour of the structures under out-of-plane loads.

Fig. 5(b) displays representative measurement curves from the experimental three-point bending tests. A direct comparison between the numerical and experimental results clearly demonstrates that the simulation accurately replicates the behaviour of the 300–30 g/m^2 and 300 g/m^2 structures, while only minor discrepancies are observed in the response of the 30 g/m^2 and 30–300 g/m^2 specimens. In the 30 g/m^2 QI structure, a higher strain of over 3 % is observed compared to the experimental value of slightly more than 2.3 %. This increased strain can be attributed to the progressive damage model CompDam and its associated pseudo-plasticity, which leads to a more gradual damage progression, especially pronounced in thinner layers. For the 30–300 g/m^2 configuration, the strength appears to be slightly underestimated in the numerical analysis.

Fig. 6(a) shows the young's modulus of the numerical and experimental three-point bending tests. This comparison shows a good agreement between the experimental and numerical results. The highest stiffness with 59.89 ± 1.18 GPa achieved by the 300 g/m^2 configuration because this configuration is slightly thicker compared to the other configurations (see Table 1). Both 30–300 g/m^2 and 300–30 g/m^2, with 52.80 ± 0.91 GPa or 52.20 ± 0.58 GPa, configurations, have similar stiffness, due to the same layup, just turned. The 30 g/m^2 has with 49.81 ± 0.65 GPa the lowest stiffness, compared to the other configurations. The stiffness distribution can be explained with the D-matrix (see Eq. (17)), where the distance of the layers to the centre axis is

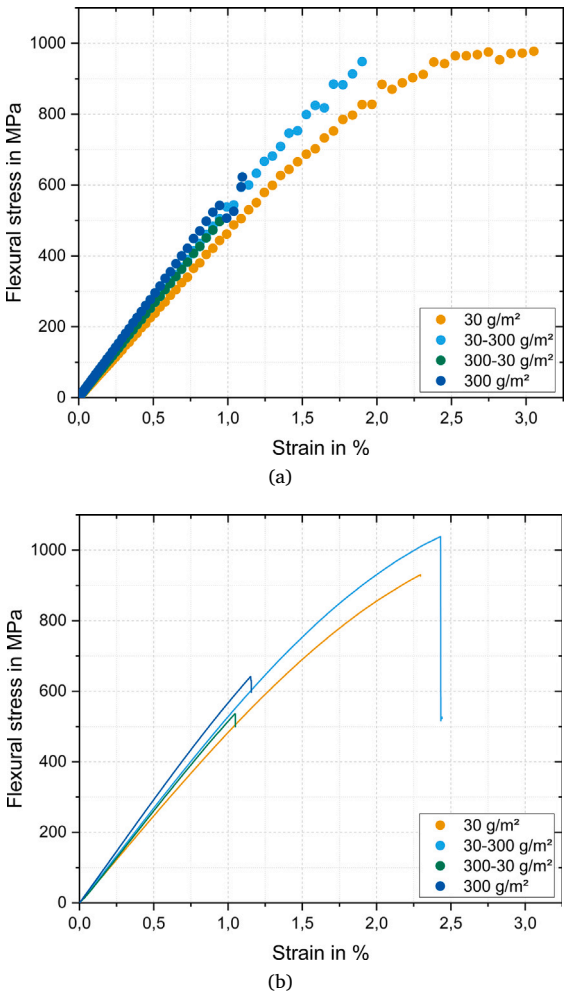

Fig. 5. Flexural strength over strain of three-point bending tests; (a) Numerical; (b) Experimental.

entered as a cube and the lower content of the 0° layer in the outer region of the laminates leads to a lower bending-stiffness.

$$\mathbf{D} = \frac{1}{3}\sum_{k=1}^{n} \bar{\mathbf{Q}}_k \cdot \left(z_k^3 - z_{k-1}^3\right) \tag{17}$$

The flexural strength of the numerical and experimental three-point bending tests is shown in Fig. 6(b). This shows that the simulation of 30 g/m^2 slightly overestimates the experimental results and that the remaining configurations are underestimated by the simulation. The observed phenomenon can be attributed to the progressive damage behaviour of CompDam and the associated pseudo-plasticity, which exhibits a more pronounced effect in thin layers. However, the comparison generally confirms that the simulation's strength prediction is largely accurate. The effect of increased bending strength with decreasing ply thickness has already been demonstrated by Yamada et al. [46]. Comparing QI laminates with fibre areal weights of 20 g/m^2 and 240 g/m^2, they reported an increase of 31.90 %. In comparison, the present study shows a similar increase of 31.78 % between QI laminates with a constant fibre areal weights of 30 g/m^2 and 300 g/m^2, which is in agreement with previously reported bending properties of thin- and thick-ply QI laminates. When comparing the averaged flexural strength of the bio-inspired 30–300 g/m^2 and 300–30 g/m^2 graded structures with the reference structures 30 g/m^2 and 300 g/m^2, it becomes clear that the 30–300 g/m^2 configuration has an improvement of 9.39 %

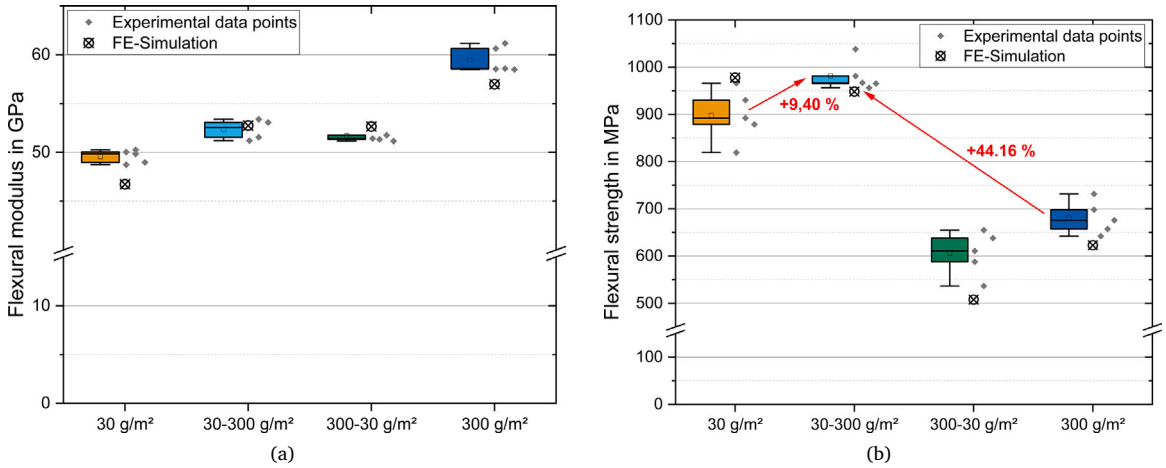

Fig. 6. Flexural properties of numerical and experimental three-point-bending test; (a) Young's modulus, (b) Flexural strength.

compared to 30 g/m^2 and 44.16 % compared to 300 g/m^2. Among all configurations, the 300–30 g/m^2 graded structure demonstrates the lowest flexural strength.

When considering the fracture patterns and mechanisms of Fig. 7 only the 30 g/m^2 fails under tensile loading (tensile fibre failure). All other configurations fail due to compression fibre failure in the compression zone, whereby those configurations with thick layers in the compression zone (300 g/m^2 and 300–30 g/m^2) to subsequently delaminate between the 0° and −45° layer. The fact that these two configurations fail under compressive loading is related to the lower compressive strength of the thick-ply QI laminates [13]. The bio-inspired 30–300 g/m^2 configuration fails under compressive loading in the compression zone despite the higher compressive strength of the thin-ply QI due to the high proportion of 0° fibre orientation of the 300 g/m^2 layer in the tension zone. This enables efficient load transfer through the fibres, leading to premature exceeding and failure of the compressive strength of the thin-ply layers.

This failure behaviour could also be accurately predicted by the numerical model. Fig. 7 presents a comparison between the numerical and experimental failure modes associated with the relevant failure mechanism. Note that in the damage images from the numerical simulation, only the inner area below the pressure fin is depicted, where active damage variables are present. Within the numerical model, the Abaqus variables FIFT and FIFC quantify fibre failure due to tension and compression in the plies. These variables range from 0, indicating that there is no damage and is represented by blue, to 1, indicating complete damage and is represented by red. The analysis clearly demonstrates that the simulation accurately predicts not only the location of the damage but also the affected layers and the type of damage. For the configurations 300 g/m^2 and 300–30 g/m^2, a clear relative displacement can be observed at the nodes between the first layer that fails under compression and the subsequent layer. This behaviour is related to the failure of the cohesive elements and corresponds to the delamination observed in the experimental failure images.

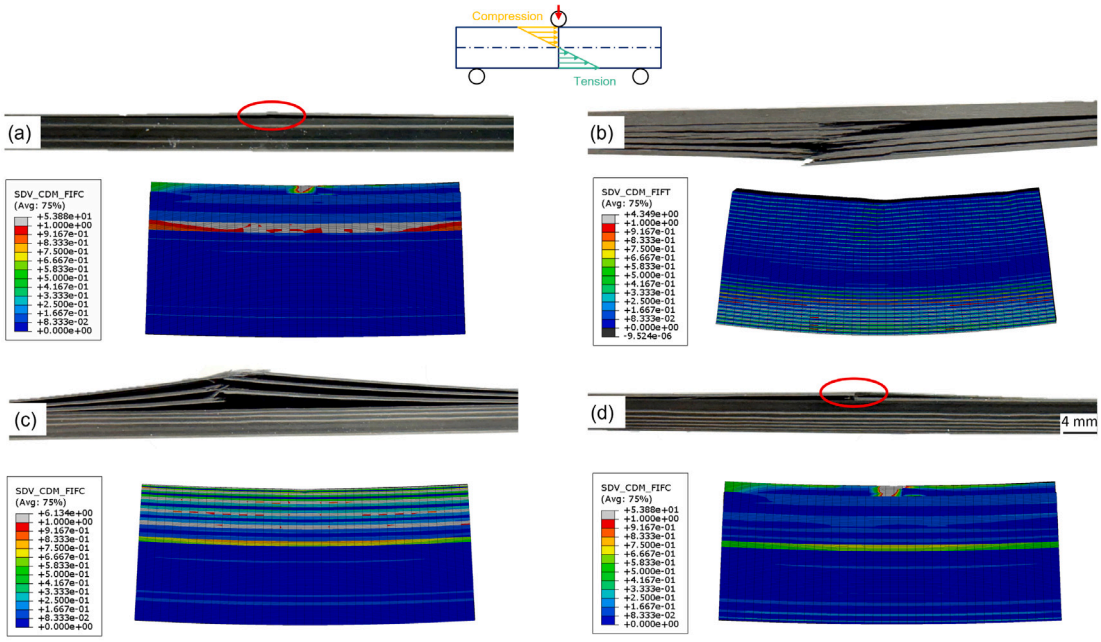

Fig. 7. Fracture patterns of numerical and experimental three point bending specimens; (a) 300 g/m^2, (b) 30 g/m^2, (c) 30–300 g/m^2 (d) 300–30 g/m^2. (For interpretation of the references to colour in this figure legend, the reader is referred to the web version of this article.)

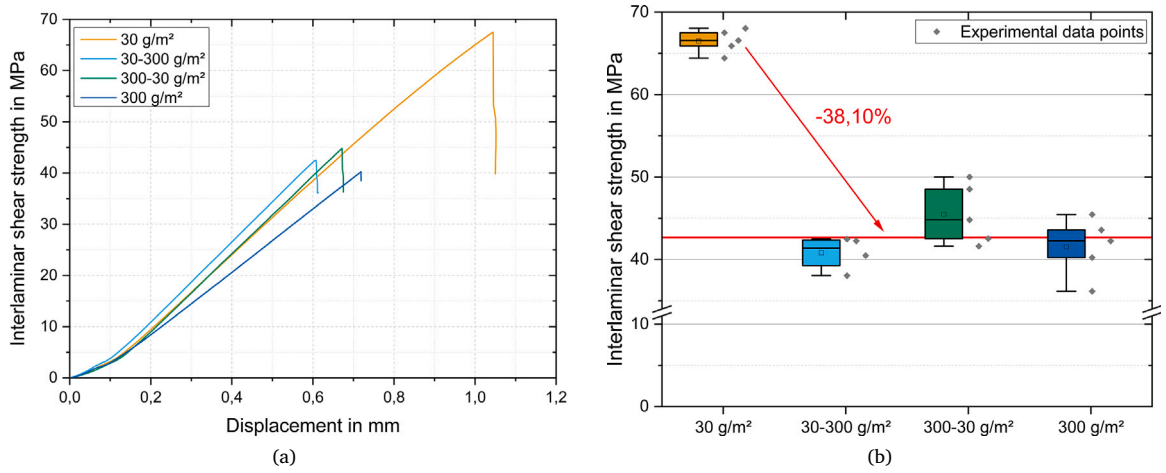

Fig. 8. Interlaminar shear strength (ILSS) of various laminate configurations: (a) ILSS as a function of displacement; (b) Statistical distribution of ILSS values presented as box plots.

3.2. Interlaminar shear strength

Representative measurement curves of the ILSS tests are presented in Fig. 8(a), while the determined apparent interlaminar shear strength is illustrated in Fig. 8(b) and summarised in Table A.5, including the mean values and standard deviations.

It can be seen that the thin-ply 30 g/m^2 achieved with 66.49 ± 1.27 MPa the highest values. All other configurations reached an averaged value of 42.74 ± 3.56 MPa which results in a 38.10 % decrease. This can be explained by the shear stress distribution in a beam subjected to bending. In a beam subjected to bending, the highest shear stresses occur in the neutral plane at the centre of the beam, while they approach zero at the edges. In between, the stress distribution can be assumed as a wide parabolic function. As shown in Fig. 9, symmetrical references with 30 g/m^2 and 300 g/m^2 fail in the middle layer area. The higher apparent interlaminar shear strength can be explained by the fact that in 30 g/m^2 laminates, the shear stresses that occur are distributed over nine times more interfaces. The ply thickness dependence of the interlaminar shear strength described here was also shown by Huang et al. [47] who reported an increase in shear strength from approximately 75.66 MPa to 80.36 MPa in their investigations on QI laminates with fibr areal weights of 125 g/m^2 and 54 g/m^2 respectively which corresponds to an improvement of nearly 13.31 %. The values reported by Huang et al. [47] are slightly higher than the apparent interlaminar shear strengths determined in this work. This difference can be attributed to the use of a toughened resin system by Huang et al. which exhibits improved shear strength compared to unmodified resin systems. Conversely, the more pronounced decrease in apparent interlaminar shear strength observed in this study is related to the use of thick-ply materials with fibre areal weights of 300 g/m^2. In contrast to a failure that occurs on the neutral axis, Fig. 9(c) shows that graded asymmetric laminate structures, shown here as an example for 30–300 g/m^2, fail in the thicker layer region near the edges, where multiple delaminations occur and are interconnected by transverse cracks. This is a logical consequence of the broad parabolic stress distribution described above. The maximum shear stress in the neutral axis layer only decreases significantly near the free edge, resulting in increased shear stress in the thicker layers. Since thicker layers exhibit lower shear strength, these structures attain apparent interlaminar shear strengths comparable to those of the reference material with 300 g/m^2.

The described effect, that graded structures fail by delamination outside the neutral axis, was also observed by Li et al. [16] in their short-beam shear tests on symmetrically graded structures. Their tests

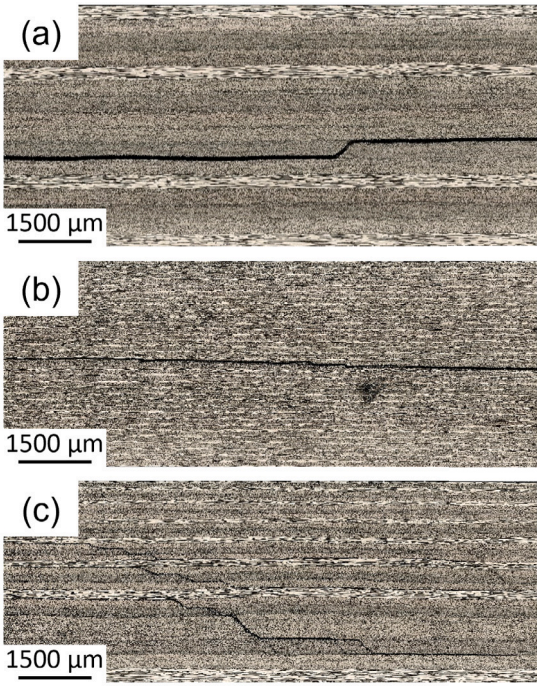

Fig. 9. Representative micrographs depicting fracture patterns of the tested ILSS specimens; (a) 300 g/m^2, (b) 30 g/m^2, (c) 30–300 g/m^2.

clearly demonstrated delamination failure occurring outside the plane. This behaviour is attributed to the use of ultra-thin ply layers in the middle region, which effectively inhibit transverse delamination cracking and thereby locally stabilise the lamination region. A similar damage pattern was also observed in the present work.

3.3. Compression after impact

All experimental data related to impact behaviour and determination of residual compressive strength, including mean values and standard deviations, are summarised in tabular form in Table A.6. Fig. 10 presents the force–time response for all tested configurations. Due to the high repeatability observed for the 30–300 g/m^2, 300–30 g/m^2, and 300 g/m^2 laminates, only a single representative curve is shown

per sample. In contrast, the 30 g/m^2 laminates exhibited different behaviours between the specimens and are therefore both plotted separately in Fig. 10(b).

Analysis of force-time curves reveals that the 30–300 g/m^2 laminate exhibits the highest peak force, closely followed by the 300 g/m^2 laminate. In laminates where the thinner layers are positioned on the opposite side of the impactor (30 g/m^2 and 300–30 g/m^2), the maximum forces observed are notably lower, suggesting a lower tolerance to damage. Moreover, the initial significant force drop, indicative of the onset of fibre breakage and marked in the diagram with a coloured line, is delayed when thinner layers are located on the non-impactor side. The effect was also identified in the studies conducted by Sasikumar et al. [22].

A closer examination of the two 30 g/m^2 specimens reveals distinct differences. Specimen 30 g/m^2-1 shows pronounced force drops, while specimen 30 g/m^2-2 exhibits a more gradual decline. Sharp force excursions typically correlate with fibre breakage, while continuous force decay is commonly associated with delamination and matrix cracks. These interpretations are corroborated by ultrasonic imaging, where the 30 g/m^2-1 specimen exhibits an extensive damage zone directly below the impact site that spans the entire thickness of the material, while the 30 g/m^2-2 specimen demonstrates larger damage regions at various depths characteristic of delamination phenomena (Fig. 11). A similar effect was observed by Kötter et al. [48]. In their study low-velocity impact tests with comparable energy levels of 2.78 J/mm^2 in the previous study compared to 3.3 J/mm^2 in the current investigation were performed. Likewise two distinct failure modes emerged. 50 % of the samples exhibited extensive failure involving one to three delaminations resulting in the formation of sublaminates while the other 50 % failed in a manner similar to the 60 g/m^2 structures with numerous delaminations interconnected by transverse cracks. The authors explained this phenomenon by proposing that the test setup lies at a critical threshold between failure modes. Another possible explanation for the observed behaviour could be the ply thickness of 30 g/m^2, which may place the material within a critical transition zone separating the two failure mechanisms.

Turning to the time–energy curves in Fig. 12, the differences between the two 30 g/m^2 specimens become indistinguishable, which justifies again presenting only one representative curve per specimen here. The most notable feature is the pronounced plateau observed for the 30 g/m^2 configuration at a relatively high energy level, indicating substantial energy absorption by the laminate. This sustained high energy absorption is indicative of extensive internal damage, consistent with the lower maximum forces recorded in Fig. 10.

In contrast, the remaining configurations return to an energy level close to zero by the end of the measurement, implying that they retained most of the impact energy after cushioning (rebound) and absorbed relatively little energy within the laminate itself.

Fig. 13 presents the results of the Compression After Impact (CAI) tests. In addition to the residual compressive strength values, the damage areas quantified by ultrasonic C-scan imaging are shown, along with the compressive strengths of the undamaged quasi-isotropic laminates (QI) laminates with 30 g/m^2 and 240 g/m^2 areal weight. The figure clearly illustrates that the damage areas of the 300 g/m^2 and 300–30 g/m^2 configurations are very close in size, which can be attributed to the 300 g/m^2 layer being oriented towards the impact side. The 30 g/m^2 configuration, however, exhibits variable behaviour, showing both larger and smaller damage areas. The underlying reasons for this variation have been discussed earlier. The smallest damage areas were observed in the 30–300 g/m^2 variant. This finding is consistent with observations by Sasikumar et al. [21–23], supporting the conclusion that unsymmetrical laminate structures with thin layers oriented towards the impacted region demonstrate greater damage tolerance under impact loading.

The CAI strengths in all the configurations tested average at 154.42 ± 10.29 MPa, with values of 168.42 ± 3.51 MPa for 30 g/m^2 and 142.62 ± 3.21 MPa for 300 g/m^2, indicating that there are no statistically significant differences in residual strength between laminates. Very similar residual strengths after impact were reported by Körbelin et al. [13] for QI laminates made from the same material system, with values of 180 MPa for 30 g/m^2 and 155 MPa for 240 g/m^2, which fall within a comparable range to those determined in this study. The impact energies used in their experiments, between 2.7 J/mm^2 and 3 J/mm^2, are also similar to the 3.3 J/mm^2 applied to the laminates tested here. The most significant difference lies in the stacking sequence of the laminates. While both studies employed QI laminates, Körbelin et al. [13] used a stacking sequence of $[45, 90, -45, 0]$, whereas this work utilised $[0, -45, 90, 45]$. It is evident that the 0° ply is located closer to the laminate core in Körbelin et al.'s [13] study, while in this work it is positioned at the outermost layer of the laminate. The influence of the 0° ply position within the laminate has been demonstrated by Nettles et al. [49] in QI face sheet honeycomb core sandwich structures. They showed that a stacking sequence of $[+45, 0, -45, 90]$ resulted in a 16 % lower CAI strength compared to a laminate stacked as $[-45, 90, +45, 0]$, attributing this difference to the location of the 0° ply. Applying these insights to the results of this study and those of Körbelin et al. [13], it becomes clear that the observed differences in residual strength can be primarily explained by the relative position of the 0° ply within the laminate structure.

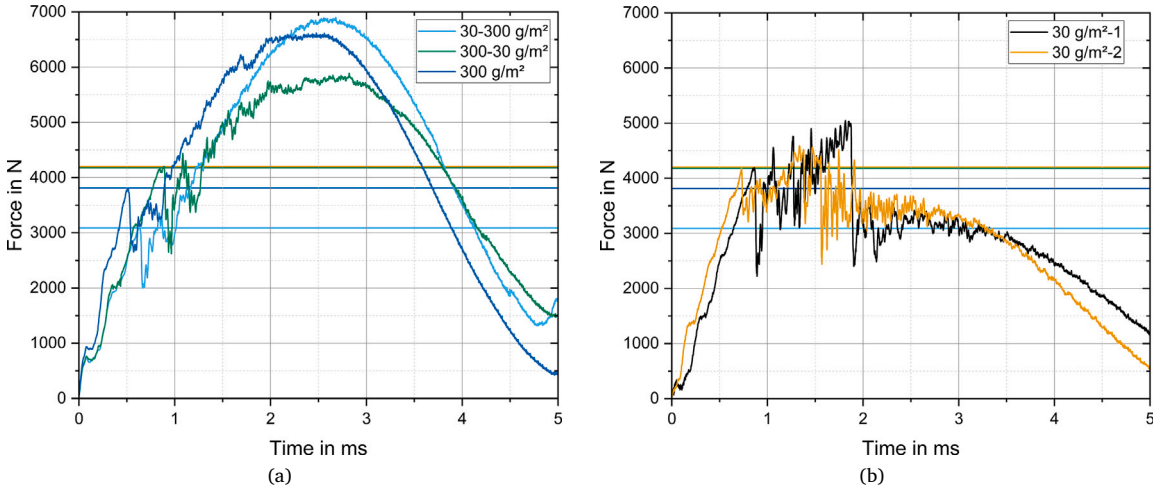

Fig. 10. Impact force-time response curves of all configurations; (a) 30–300 g/m^2, 300–30 g/m^2, 300 g/m^2; (b) 30 g/m^2.

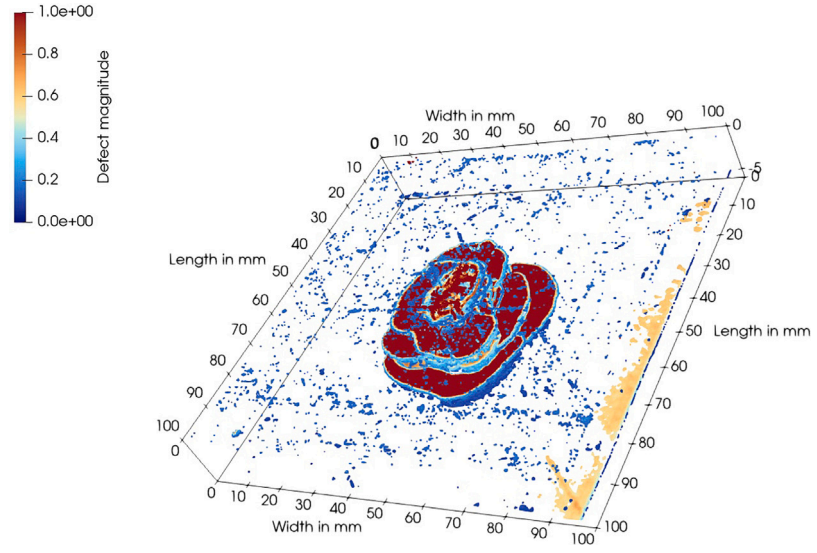

(a)

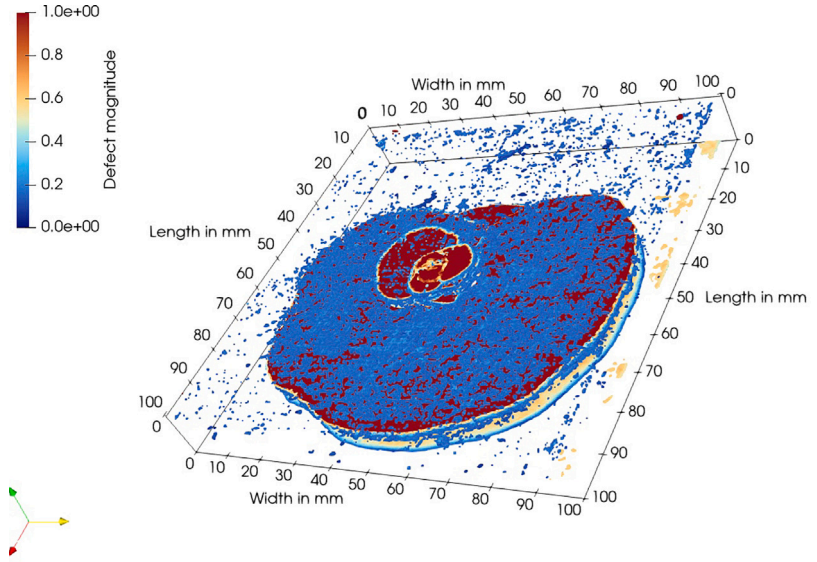

(b)

Fig. 11. Impact damage patterns detected using ultrasonic technique; (a) 30 g/m^2-1, (b) 30 g/m^2-2.

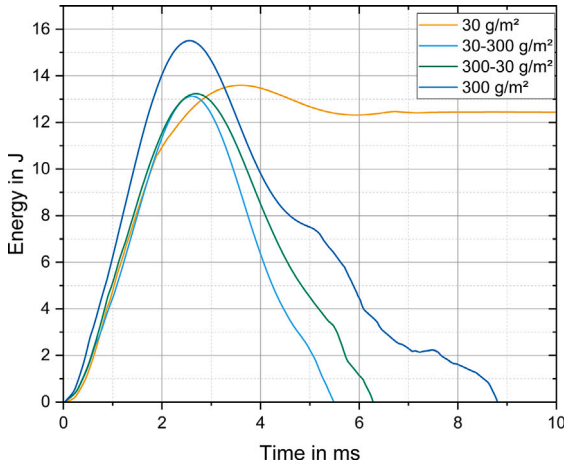

Fig. 12. Impact energy evolution curves of all laminates.

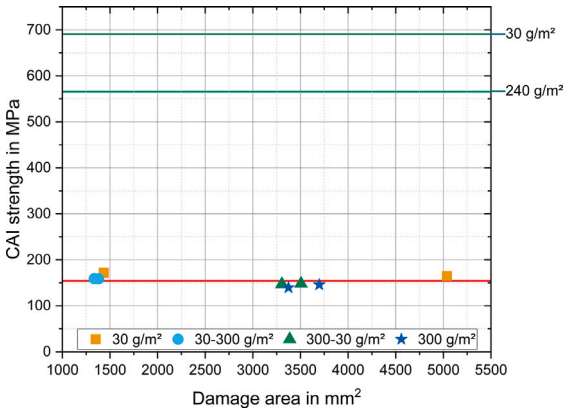

Fig. 13. Compression-after-impact strength in relation to damage area, together with undamaged compression strength of quasi-isotropic laminate structures with 30 g/m^2 and 240 g/m^2 [13].

The observation that there is no significant change in CAI strength between the different configurations can be attributed to the fact that the undamaged compressive strength of QI thin-ply laminates (30 g/m^2) is substantially higher (690.73 MPa) compared to thick-ply laminates (240 g/m^2), which exhibit a compressive strength of 565.63 MPa [13]. However, as shown in Fig. 12, thin-ply laminates absorb considerably more impact energy, resulting in more severe damage. In the present study, these opposing effects appear to balance each other, leading to comparable residual strengths in all configurations.

Nevertheless, compared to the respective undamaged compressive strengths, laminates exhibit a reduction in residual strength of approximately 77.64 % for the 30 g/m^{2}configuration and 72.70 % for the 240 g/m^2 configuration, highlighting the substantial impact-induced degradation in compressive performance.

4. Conclusion

This study demonstrates that the generalised design approach of combining variable layer thicknesses in graded laminates with a B-matrix of zero successfully prevents thermal distortion after manufacturing. The combination of different layer thicknesses leads to a significant increase in flexural strength, with the bio-inspired concept enabling an increase of up to 44.16 % compared to the 300 g/m^2 laminate and 9.39 % compared to the 30 g/m^2 laminate.

Validation through numerical FEM simulations demonstrated strong agreement with the experimental results and facilitated an efficient analysis of laminate structures, including identification of damage types, their precise location, and affected layers.

At the same time, it was found that the apparent interlaminar shear strengths are significantly influenced by the thickest layer, resulting in an average 38.10 % lower strength compared to the 30 g/m^2 reference, an effect that can be explained by the distribution of parabolic shear stress across thickness.

Impact tests showed that the 30–300 g/m^2 configuration had the smallest damaged areas and was therefore particularly tolerant to damage. However, the compression after impact tests did not demonstrate a clear advantage for either configuration, as thin-ply laminates exhibited more extensive damage due to higher energy absorption, while thick-ply laminates showed reduced compressive strength.

In summary, the results demonstrate that the lobster configuration, characterised by thin layers on the front loading side and thick layers on the rear loading side, contributes to increased flexural strength and reduced damage area after impact loading. These findings highlight the potential of bio-inspired graded laminate designs to enhance mechanical performance, supporting their future implementation in engineering applications where flexural strength and damage tolerance are critical.

CRediT authorship contribution statement

Marcel Neubacher: Writing – original draft, Visualization, Validation, Methodology, Investigation, Formal analysis, Conceptualization. **Farida Touni:** Writing – review & editing, Visualization, Methodology, Investigation. **Kohei Yamada:** Writing – review & editing, Methodology, Investigation. **Masaaki Nishikawa:** Writing – review & editing, Supervision, Project administration, Funding acquisition. **Bodo Fiedler:** Writing – review & editing, Supervision, Project administration, Methodology, Investigation, Funding acquisition, Conceptualization.

Declaration of competing interest

The authors declare that they have no known competing financial interests or personal relationships that could have appeared to influence the work reported in this paper.

Acknowledgements

The authors appreciate the support of the DAAD, Germany (Project: 57710630) and the German Research Foundation, Germany (DFG, project number 513556749) for funding this project. The authors acknowledge support for Open Access publishing by the Projekt DEAL agreement, Germany and the Hamburg University of Technology (TUHH). The authors thank all contributing colleagues from the Institute of Polymers and Composites for their support.

Appendix. Example appendix section

See Tables A.5–A.7.

Table A.5
Apparent interlaminar shear strength with mean values and standard deviations

Configuration	Apparent interlaminar shear strength
30 g/m^2	66.49 ± 1.27 MPa
30–300 g/m^2	41.16 ± 1.78 MPa
300–30 g/m^2	45.50 ± 3.28 MPa
300 g/m^2	41.53 ± 3.19 MPa

Table A.6
Damage area after impact and corresponding CAI strength with mean values and standard deviations

Configuration	Damage area	CAI strength
30 g/m^2	3234.97 ± 1801.27 mm^2	168.42 ± 3.51 MPa
30–300 g/m^2	1358.07 ± 22.72 mm^2	158.94 ± 0.12 MPa
300–30 g/m^2	3405.71 ± 100.48 mm^2	147.70 ± 0.57 MPa
300 g/m^2	3536.23 ± 161.50 mm^2	142.62 ± 3.21 MPa

Table A.7
Mechanical properties determined by three-point bending test including mean values and standard deviations for experimental and numerical data

Configuration	Numerical young's modulus	Experimental young's modulus	Numerical flexural strength	Experimental flexural strength
30 g/m^2	46.27 GPa	49.81 ± 0.65 GPa	977.80 MPa	897.40 ± 49.61 MPa
30–300 g/m^2	52.20 GPa	52.80 ± 0.91 GPa	948.41 MPa	981.69 ± 29.46 MPa
300–30 g/m^2	52.01 GPa	52.20 ± 0.58 GPa	507.70 MPa	605.58 ± 41.44 MPa
300 g/m^2	56.02 GPa	59.89 ± 1.18 GPa	622.87 MPa	680.98 ± 31.48 MPa

Data availability

Data will be made available on request.

References

[1] Grunenfelder L, Suksangpanya N, Salinas C, Milliron G, Yaraghi N, Herrera S, Evans-Lutterodt K, Nutt S, Zavattieri P, Kisailus D. Bio-inspired impact-resistant composites. Acta Biomater 2014;10(9):3997–4008. http://dx.doi.org/10.1016/j.actbio.2014.03.022, URL https://linkinghub.elsevier.com/retrieve/pii/S1742706114001330.

[2] Miserez A, Weaver JC, Thurner PJ, Aizenberg J, Dauphin Y, Fratzl P, Morse DE, Zok FW. Effects of laminate architecture on fracture resistance of sponge biosilica: Lessons from nature. Adv Funct Mater 2008;18(8):1241–8. http://dx.doi.org/10.1002/adfm.200701135, URL https://onlinelibrary.wiley.com/doi/10.1002/adfm.200701135.

[3] Monn MA, Weaver JC, Zhang T, Aizenberg J, Kesari H. New functional insights into the internal architecture of the laminated anchor spicules of *Euplectella aspergillum*. Proc Natl Acad Sci 2015;112(16):4976–81. http://dx.doi.org/10.1073/pnas.1415502112, URL https://pnas.org/doi/full/10.1073/pnas.1415502112.

[4] Fabritius H-O, Sachs C, Triguero PR, Raabe D. Influence of structural principles on the mechanics of a biological fiber-based composite material with hierarchical organization: The exoskeleton of the lobster *Homarus americanus*. Adv Mater 2009;21(4):391–400. http://dx.doi.org/10.1002/adma.200801219, URL https://onlinelibrary.wiley.com/doi/10.1002/adma.200801219.

[5] Mendoza-Galván A, Del Río LF, Järrendahl K, Arwin H. Graded pitch profile for the helicoidal broadband reflector and left-handed circularly polarizing cuticle of the scarab beetle Chrysina chrysargyrea. Sci Rep 2018;8(1):6456. http://dx.doi.org/10.1038/s41598-018-24761-w, URL https://www.nature.com/articles/s41598-018-24761-w.

[6] Romano P, Fabritius H, Raabe D. The exoskeleton of the lobster Homarus americanus as an example of a smart anisotropic biological material. Acta Biomater 2007;3(3):301–9. http://dx.doi.org/10.1016/j.actbio.2006.10.003, URL https://linkinghub.elsevier.com/retrieve/pii/S1742706106001449.

[7] Sihn S, Kim R, Kawabe K, Tsai S. Experimental studies of thin-ply laminated composites. Compos Sci Technol 2007;67(6):996–1008. http://dx.doi.org/10.1016/j.compscitech.2006.06.008, URL https://linkinghub.elsevier.com/retrieve/pii/S0266353806002168.

[8] Kawabe K, Tomoda S, Matsuo T. Pneumatic process for spreading reinforcing fiber tow. In: International SAMPE symposium and exhibition. proceedings, vol. 42, 1997, p. 65–76, URL https://www.scopus.com/inward/record.uri?eid=2-s2.0-0030719589&partnerID=40&md5=1a2998a96b72aae5587902e3b1b66023. Issue: 1 Type: Conference paper.

[9] Arteiro A, Furtado C, Catalanotti G, Linde P, Camanho P. Thin-ply polymer composite materials: A review. Compos A 2020;132:105777. http://dx.doi.org/10.1016/j.compositesa.2020.105777, URL https://linkinghub.elsevier.com/retrieve/pii/S1359835X20300154.

[10] Arteiro A, Catalanotti G, Xavier J, Camanho P. Notched response of non-crimp fabric thin-ply laminates. Compos Sci Technol 2013;79:97–114. http://dx.doi.org/10.1016/j.compscitech.2013.02.001, URL https://linkinghub.elsevier.com/retrieve/pii/S0266353813000390. Publisher: Elsevier BV.

[11] Amacher R, Cugnoni J, Botsis J, Sorensen L, Smith W, Dransfeld C. Thin ply composites: Experimental characterization and modeling of size-effects. Compos Sci Technol 2014;101:121–32. http://dx.doi.org/10.1016/j.compscitech.2014.06.027, URL https://linkinghub.elsevier.com/retrieve/pii/S0266353814002280.

[12] Amacher R, Cugnoni J, Botsis J. Thin ply composites: experimental characterization and modeling. In: The 19th international conference on composite materials. 2013.

[13] Körbelin J, Kötter B, Voormann H, Brandenburg L, Selz S, Fiedler B. Damage tolerance of few-layer graphene modified CFRP: From thin-to thick-ply laminates. Compos Sci Technol 2021;209:108765. http://dx.doi.org/10.1016/j.compscitech.2021.108765, URL https://linkinghub.elsevier.com/retrieve/pii/S0266353821001214.

[14] Loukil MS, Costa S, Bergwall M, Deepthi Prasad H, Moreau F, Segersäll M, Kapidzic Z, Olsson R. Experimental and numerical investigation on bearing behavior of hybrid thin/thick-ply composite laminates. Compos Struct 2024;331:117888. http://dx.doi.org/10.1016/j.compstruct.2024.117888, URL https://linkinghub.elsevier.com/retrieve/pii/S0263822324000163.

[15] Furtado C, Arteiro A, Catalanotti G, Xavier J, Camanho P. Selective ply-level hybridisation for improved notched response of composite laminates. Compos Struct 2016;145:1–14. http://dx.doi.org/10.1016/j.compstruct.2016.02.050, URL https://linkinghub.elsevier.com/retrieve/pii/S0263822316300915.

[16] Li X, Yuan Y. Hybrid and gradient design of ultra-thin-ply composite laminates for synergistic suppression of delamination and fiber fracture damage modes. Eng Fract Mech 2024;295:109822. http://dx.doi.org/10.1016/j.engfracmech.2023.109822, URL https://linkinghub.elsevier.com/retrieve/pii/S0013794423007804.

[17] Li X, Yuan Y, Zhang Z. Gradient ply thickness design for enhanced low-velocity impact resistance in ultra-thin ply composite. Extrem Mech Lett 2023;63:102054. http://dx.doi.org/10.1016/j.eml.2023.102054, URL https://linkinghub.elsevier.com/retrieve/pii/S2352431623001001.

[18] Sasikumar A, Costa J, Trias D, Llobet J, Cózar I, Turon A, Linde P. A virtual testing based search for optimum compression after impact strength in thin laminates using ply-thickness hybridization and unsymmetrical designs. Compos Sci Technol 2020;196:108188. http://dx.doi.org/10.1016/j.compscitech.2020.108188, URL https://linkinghub.elsevier.com/retrieve/pii/S0266353819333743.

[19] Sasikumar A, Trias D, Costa J, Blanco N, Orr J, Linde P. Effect of ply thickness and ply level hybridization on the compression after impact strength of thin laminates. Compos A 2019;121:232–43. http://dx.doi.org/10.1016/j.compositesa.2019.03.022, URL https://linkinghub.elsevier.com/retrieve/pii/S1359835X19301010.

[20] Sebaey T, Mahdi E. Using thin-plies to improve the damage resistance and tolerance of aeronautical CFRP composites. Compos A 2016;86:31–8. http://dx.doi.org/10.1016/j.compositesa.2016.03.027, URL https://linkinghub.elsevier.com/retrieve/pii/S1359835X16300446.

[21] Sasikumar A, Trias D, Costa J, Singery V, Linde P. Mitigating the weak impact response of thin-ply based thin laminates through an unsymmetrical laminate design incorporating intermediate grade plies. Compos Struct 2019;220:93–104. http://dx.doi.org/10.1016/j.compstruct.2019.03.069, URL https://linkinghub.elsevier.com/retrieve/pii/S0263822318347032.

[22] Sasikumar A, Costa J, Trias D, González E, García-Rodríguez S, Maimí P. Unsymmetrical stacking sequences as a novel approach to tailor damage resistance under out-of-plane impact loading. Compos Sci Technol 2019;173:125–35. http://dx.doi.org/10.1016/j.compscitech.2019.02.002, URL https://linkinghub.elsevier.com/retrieve/pii/S026635381831710X.

[23] Sasikumar A, García-Rodríguez S, Arbeláez J, Trias D, Costa J. On how unsymmetrical laminate designs with tailored ply clusters affect compression after impact strength compared to symmetric baseline. Compos Struct 2020;238:111958. http://dx.doi.org/10.1016/j.compstruct.2020.111958, URL https://linkinghub.elsevier.com/retrieve/pii/S0263822319316836.

[24] Malekinejad H, Carbas RJC, Akhavan-Safar A, Marques EAS, Ferreira M, Da Silva LFM. Bio-inspired helicoidal composite structure featuring graded variable ply pitch under transverse tensile loading. J Compos Sci 2024;8(6):228. http://dx.doi.org/10.3390/jcs8060228, URL https://www.mdpi.com/2504-477X/8/6/228.

[25] Luo H, Wang H, Zhao Z, Xue H, Li Y. Experimental and numerical investigation on the failure behavior of Bouligand laminates under off-axis open-hole tensile loading. Compos Struct 2023;313:116932. http://dx.doi.org/10.1016/j.compstruct.2023.116932, URL https://linkinghub.elsevier.com/retrieve/pii/S0263822323002763.

[26] Wang H, Wang C, Hazell PJ, Wright A, Zhang Z, Lan X, Zhang K, Zhou M. Insights into the high-velocity impact behaviour of bio-inspired composite laminates with helicoidal lay-ups. Polym Test 2021;103:107348. http://dx.doi.org/10.1016/j.polymertesting.2021.107348, URL https://linkinghub.elsevier.com/retrieve/pii/S0142941821002932.

[27] Sharma A, Shukla NK, Belarbi M-O, Abbas M, Garg A, Li L, Bhutto J, Bhatia A. Bio-inspired nacre and helicoidal composites: From structure to mechanical applications. Thin-Walled Struct 2023;192:111146. http://dx.doi.org/10.1016/j.tws.2023.111146, URL https://linkinghub.elsevier.com/retrieve/pii/S0263823123006249.

[28] Körbelin J, Goralski P, Kötter B, Bittner F, Endres H-J, Fiedler B. Damage tolerance and notch sensitivity of bio-inspired thin-ply Bouligand structures. Compos C 2021;5:100146. http://dx.doi.org/10.1016/j.jcomc.2021.100146, URL https://linkinghub.elsevier.com/retrieve/pii/S2666682021000414.

[29] Neubacher M, Touni F, Yamada K, Nishikawa M, Fiedler B. Coelacanth-scale inspired thin-ply composites for load-bearing applications. Compos C 2025;100667. http://dx.doi.org/10.1016/j.jcomc.2025.100667, URL https://linkinghub.elsevier.com/retrieve/pii/S2666682025001094.

[30] Zhang X, Yuan Y. Bioinspired hybrid helical structure in lobster Homarus Americanus: Enhancing penetration resistance and protective performance. Compos A 2024;177:107927. http://dx.doi.org/10.1016/j.compositesa.2023.107927, URL https://linkinghub.elsevier.com/retrieve/pii/S1359835X23005031.

[31] Greenfeld I, Wagner HD. Two natural toughening strategies may inspire sustainable structures. Sci Rep 2023;13(1):20416. http://dx.doi.org/10.1038/s41598-023-47574-y, URL https://www.nature.com/articles/s41598-023-47574-y.

[32] Kötter B, Yamada K, Takatsuka N, Fiedler B, Nishikawa M. Numerical investigation of the bearing performance of Thin- and Thick-Ply hybrid laminates. Compos Struct 2024;345:118372. http://dx.doi.org/10.1016/j.compstruct.2024.118372, URL https://linkinghub.elsevier.com/retrieve/pii/S0263822324005002.

[33] Camanho P, Tavares C, De Oliveira R, Marques A, Ferreira A. Increasing the efficiency of composite single-shear lap joints using bonded inserts. Compos B 2005;36(5):372–83. http://dx.doi.org/10.1016/j.compositesb.2005.01.007, URL https://linkinghub.elsevier.com/retrieve/pii/S1359836805000235.

[34] Davila C, Jaunky N, Goswami S. Failure criteria for frp laminates in plane stress. In: 44th AIAA/ASME/ASCE/AHS/ASC structures, structural dynamics, and materials conference. Norfolk, Virginia: American Institute of Aeronautics and Astronautics; 2003, http://dx.doi.org/10.2514/6.2003-1991, URL http://arc.aiaa.org/doi/10.2514/6.2003-1991.

[35] Wanthal SP, Schaefer JD, Justusson BP, Hyder I, Engelstad SP, Rose CA. Paper number: Session topic: Verification & validation of progressive damage/failure analysis for stiffened composite structures title: Verification and validation process for progressive damage and failure analysis methods in the NASA advanced composites consortium. 2017, URL https://api.semanticscholar.org/CorpusID:109933164.

[36] Leone FA, Bergan AC, Dávila CG. CompDam - deformation gradient decomposition (DGD), v2.5.0. 2019, URL https://github.com/nasa/CompDam_DGD.

[37] Catalanotti G, Camanho P, Xavier J, Dávila C, Marques A. Measurement of resistance curves in the longitudinal failure of composites using digital image correlation. Compos Sci Technol 2010;70(13):1986–93. http://dx.doi.org/10.1016/j.compscitech.2010.07.022, URL https://linkinghub.elsevier.com/retrieve/pii/S0266353810002915.

[38] Lu X, Ridha M, Chen B, Tan V, Tay T. On cohesive element parameters and delamination modelling. Eng Fract Mech 2019;206:278–96. http://dx.doi.org/10.1016/j.engfracmech.2018.12.009, URL https://linkinghub.elsevier.com/retrieve/pii/S0013794418308609.

[39] Körbelin J, Junge N, Fiedler B. Modelling of low-velocity impact and compression after impact of CFRP at elevated temperatures. Compos A 2021;147:106418. http://dx.doi.org/10.1016/j.compositesa.2021.106418, URL https://linkinghub.elsevier.com/retrieve/pii/S1359835X2100141X.

[40] Pedro J, Gonçalves P, Soares G, Arteiro A, Honke R, Karch C. Mechanical loads from simulated lightning strike on protected carbon fibre-reinforced polymers revisited: implementation and experimental validation. Aeronaut J 2025;1–33. http://dx.doi.org/10.1017/aer.2025.10055, URL https://www.cambridge.org/core/product/identifier/S0001924025100559/type/journal_article.

[41] DIN EN ISO 14125 faserverstärkte kunststoffe – bestimmung der biegeeigenschaften. 2011, http://dx.doi.org/10.31030/1753441.

[42] Pinho ST, Dávila CG, Camanho PP, Iannucci L, Robinson P. Failure models and criteria for FRP under in-plane or three-dimensional stress states including shear non-linearity. Tech. rep., 2013, URL https://ntrs.nasa.gov/citations/20050110223.

[43] DIN EN ISO 14130 Bestimmung der scheinbaren interlaminaren Scherfestigkeit nach dem Dreipunktverfahren mit kurzem Balken. 1998, http://dx.doi.org/10.31030/7433990.

[44] ASTM D 7136-05 standard test method for measuring the damage resistance of a fiber-reinforced polymer matrix composite to a drop-weight impact event. 2005.

[45] ASTM D 7137-05 standard test method for compressive residual strength properties of damaged polymer matrix composite plates. 2005.

[46] Yamada K, Kawabe K, Yamamoto S, Matsuda N, Nishikawa M, Hojo M. Effect of ply thickness and matrix resin on flexural properties of thin ply CFRP laminates. J Jpn Soc Compos Mater 2019;45(2):61–71. http://dx.doi.org/10.6089/jscm.45.61, URL https://www.jstage.jst.go.jp/article/jscm/45/2/45_61/_article/-char/ja/.

[47] Huang C, Jiang D, He M, Xiao J, Zheng Q, Ju S. Study on the strength of thin-ply laminates of cfrp under interlaminar shear loadings. Munich; 2016.

[48] Kötter B, Endres J, Körbelin J, Bittner F, Endres H-J, Fiedler B. Fatigue and fatigue after impact behaviour of Thin- and Thick-Ply composites observed by computed tomography. Compos C 2021;5:100139. http://dx.doi.org/10.1016/j.jcomc.2021.100139, URL https://linkinghub.elsevier.com/retrieve/pii/S2666682021000347.

[49] Nettles AT, Barnes BW, Guin WE, Mavo JP. The effects of off-axis loading on the compression after impact strength of quasi-isotropic face sheet honeycomb core sandwich structure. J Sandw Struct Mater 2023;25(7):793–802. http://dx.doi.org/10.1177/10996362231180147, URL https://journals.sagepub.com/doi/10.1177/10996362231180147.